AGU ADVANCING EARTH AND SPACE SCIENCE

Geochemistry, Geophysics, Geosystems

RESEARCH ARTICLE
10.1029/2021GC009638

Key Points:

- Biomarker thermal maturity shows that the Pāpaku fault, a large splay fault of the Hikurangi subduction zone, has hosted large (~>M_w 7) earthquakes along multiple fault strands
- The Pāpaku fault and other splay faults along the Hikurangi margin are associated with high earthquake and tsunami hazard
- We document evidence of near-seafloor, 14–17 m of earthquake slip in four areas within the upper 40 m of the fault zone

Supporting Information:

Supporting Information may be found in the online version of this article.

Correspondence to:

G. L. Coffey,
g.coffey@gns.cri.nz

Citation:

Coffey, G. L., Savage, H. M., Polissar, P. J., Meneghini, F., Ikari, M. J., Fagereng, Å., et al. (2021). Evidence of seismic slip on a large splay fault in the Hikurangi subduction zone. *Geochemistry, Geophysics, Geosystems*, *22*, e2021GC009638. https://doi.org/10.1029/2021GC009638

Received 21 JAN 2021
Accepted 10 APR 2021

Evidence of Seismic Slip on a Large Splay Fault in the Hikurangi Subduction Zone

Genevieve L. Coffey[1], Heather M. Savage[2], Pratigya J. Polissar[2], Francesca Meneghini[3], Matt J. Ikari[4], Åke Fagereng[5], Julia K. Morgan[6], and Maomao Wang[7]

[1]GNS Science, Earth Structure and Processes, Lower Hutt, New Zealand, [2]Division of Earth and Planetary Sciences, University of California Santa Cruz, Santa Cruz, CA, USA, [3]Department of Earth Sciences, University of Pisa, Pisa, Italy, [4]MARUM Center for Marine Environmental Sciences and Faculty of Geosciences, University of Bremen, Bremen, Germany, [5]School of Earth and Environmental Sciences, Cardiff University, Cardiff, UK, [6]Department of Earth, Environmental and Planetary Sciences, Rice University, Houston, TX, USA, [7]College of Oceanography, Hohai University, Nanjing, China

Abstract The Hikurangi subduction zone is capable of producing moderate to large earthquakes as well as regularly repeating slow slip events. However, it is unclear what structures host these different slip styles along the margin. Here we address whether splay faults can host seismic slip at shallow (<1 km) depth by investigating the Pāpaku fault, sampled during International Ocean Discovery Program Expedition 375. We use biomarker thermal maturity to search for evidence of frictional heating within turbiditic sediments of the Pāpaku fault. Four zones of localized high temperature are found near the top of the fault zone, which are interpreted to be zones of localized seismic slip. Thermal modeling shows that the most likely maximum displacement on the shallow Pāpaku fault during each event was 14–17 m. Our results demonstrate that the Pāpaku fault, and potentially other splay faults along the margin, host coseismic slip and have the potential to produce large tsunami (e.g., runup heights of >1 m as observed in the 1947 Poverty and Tolaga Bay earthquakes.

1. Introduction

Subduction zones are capable of producing the largest earthquakes on Earth and as such, are associated with high seismic hazard and tsunamigenic potential. Determining how strain is accommodated across subduction zones, including the plate boundary and accretionary wedge faults, is necessary to better assess their seismic potential. However, understanding earthquake slip in these regions is complicated by subduction zone heterogeneity, such as lithological variation, deformation in the upper plate, and seafloor topography (Barker et al., 2018; Barnes et al., 2020; Bécel et al., 2017; Bell et al., 2010; Kimura et al., 2007; Wang & Bilek, 2014). Furthermore, slower slip also occurs along subduction faults, for instance slow slip events, low frequency earthquakes, and tremor, which influence coupling and strain release over time (Obara & Kato, 2016; Peng & Gomberg, 2010; Saffer & Wallace, 2015; Shaddox & Schwartz, 2019; Wallace & Beavan, 2010; Wallace et al., 2004, 2009; Wech & Creager, 2011). To accurately understand the hazard posed by subduction zones, it is necessary to determine how the associated faults participate in the earthquake cycle.

The Hikurangi subduction zone extends offshore of the eastern edge of the North Island of New Zealand and accommodates convergence between the Pacific and Australian plates at a rate of ~57.6 mm/year in the north, which decreases to a rate of 22.3 mm/year at the southern end of the margin (Wallace & Beavan, 2010). Shallow and deep slow slip events regularly occur along the northern and southern ends of the margin, respectively (e.g., McCaffrey et al., 2008; Wallace & Beavan, 2010; Wallace et al., 2016), and play a fundamental role in relieving elastic strain along the subduction interface (Wallace et al., 2009). In addition, historic and geologic evidence demonstrates that moderate to large earthquakes occur at the Hikurangi Margin (Berryman et al., 1989, 2011; Clark et al., 2019; Ota et al., 1991; Pouderoux et al., 2014; Wilson et al., 2006). Notable earthquakes, that may have involved slip on the subduction thrust interface and/or splay faults rooting from it, include the 1947 Tolaga Bay and Poverty Bay earthquakes (Figure 1). These M_w 7 events were tsunami earthquakes with low shaking intensity and slow rupture velocity (Bell et al., 2014; Bilek & Lay, 2002; Johnson & Satake, 1997). Although the evidence of a wide spectrum of slip velocities at

10.1029/2021GC009638

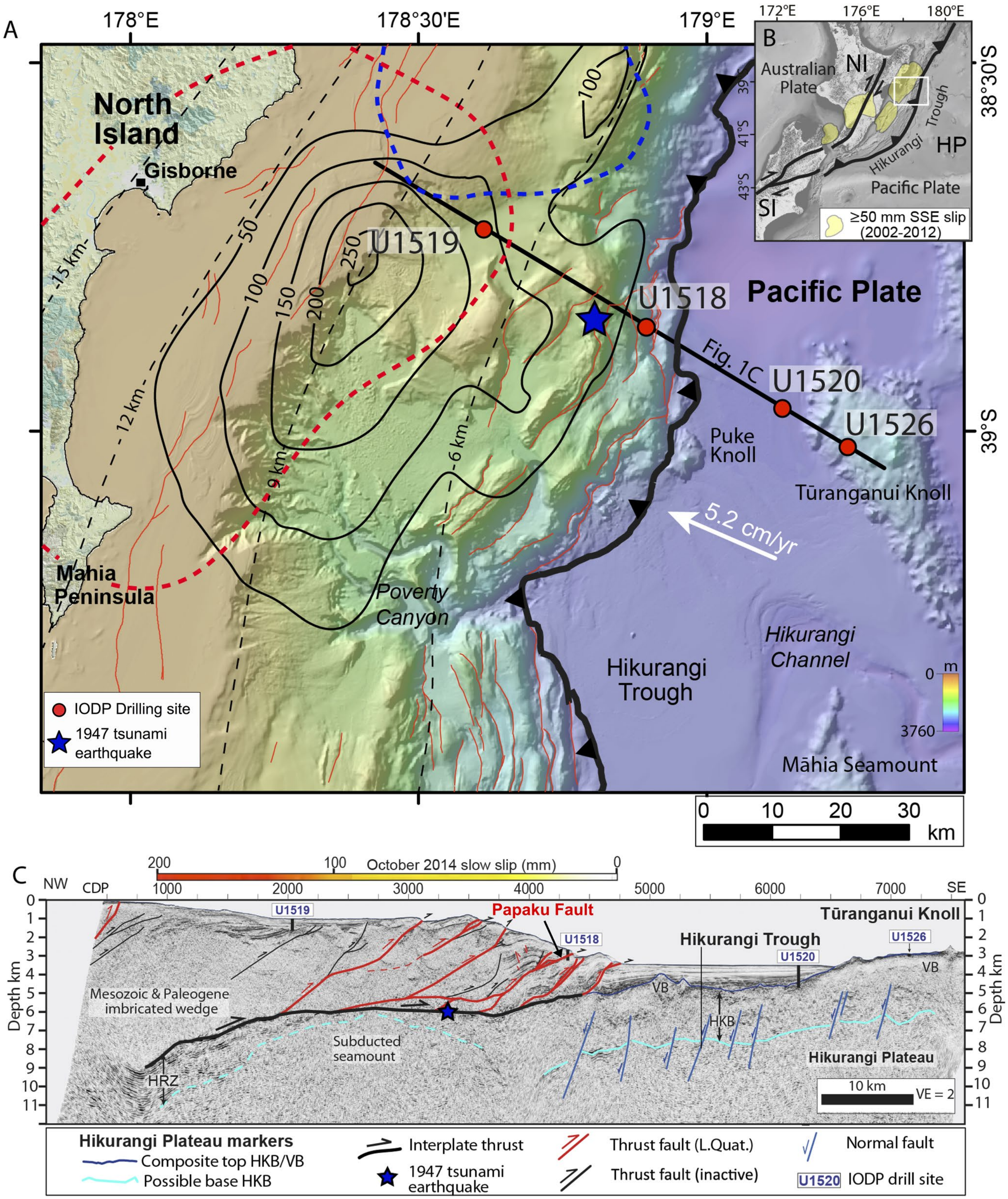

Figure 1. Overview of the northern Hikurangi subduction zone from Barnes et al. (2020). (a) Bathymetry of the northern Hikurangi margin showing the extent of recent slow slip events and the location of sites drilled during International Ocean Discovery Program (IODP) EXP375. (b) Location of the study site offshore of the eastern North Island. (c) Seismic profile along the bold black line indicated in (a) showing upper plate structure at the northern Hikurangi margin where drilling occurred.

10.1029/2021GC009638

the Hikurangi margin is well documented, the exact structures that participate in slip events of different speeds over geologic time are unclear.

International Ocean Discovery Program (IODP) expeditions 372/375 drilled and logged through the accretionary wedge of the Hikurangi subduction zone and collected core at four sites (Figure 1a). Site U1518 cored through the Pāpaku fault, one of numerous reverse faults along the margin that splay off the megathrust (Bell et al., 2010; Fagereng et al., 2019). Paleoseismic and coring studies infer earthquake slip along splay faults in New Zealand (Ota et al., 1991; Pouderoux et al., 2014), and elsewhere (e.g., NantroSEIZE; Hayman et al., 2012). While some of these studies demonstrate evidence of coseismic heating (Sakaguchi et al., 2011), we still lack direct evidence of large earthquakes on these structures in New Zealand. Coseismic displacement along splay faults like the Pāpaku fault, which are more steeply dipping than the megathrust, have greater potential for tsunamigenesis (Moore et al., 2007; Wendt et al., 2009). Here, we investigate the seismic history of the Pāpaku fault by measuring biomarker thermal maturity on samples from U1518 as a proxy for frictionally generated temperature rise during seismic slip. We identify thermally mature samples within the Pāpaku fault zone and constrain the temperatures and displacements required for reaction at a range of slip velocities consistent with both tsunami and regular earthquakes.

2. Background and Methods

2.1. The Pāpaku Fault

Rooted in the megathrust decollement (Figure 1c), the Pāpaku fault extends through the accretionary prism up to the seafloor and has hosted ~6 km of total displacement (Barker et al., 2018). It can broadly be split into the older and more consolidated hanging wall, the highly deformed, footwall-derived fault zone, and the footwall. We consider the entire fault zone together here, although it can be further divided by the distribution of deformation into an upper main fault (304–322 m below sea floor, mbsf), a lower subsidiary fault (351–361 mbsf), and a region of less-intense deformation between the two (Fagereng et al., 2019). Evidence of mixed-mode deformation is pervasive throughout the fault zone and includes fractures, faulting, flow structures, and folding. Such a range of structures is consistent with the fault slipping at different strain rates or different effective normal stress (Fagereng et al., 2019).

2.2. Biomarker Paleothermometry on Faults

During an earthquake, frictional resistance along a fault can lead to the generation of very high transient temperatures, sometimes high enough to melt rock and produce pseudotachylyte (Sibson, 1975). The temperature rise that occurs is related to properties of the fault rock as well as the earthquake source (Lachenbruch, 1986):

$$\Delta T \propto \frac{\tau}{\rho c_p}\frac{vt}{2a} \tag{1}$$

where, τ is shear stress, ρ is density, c_p is heat capacity, v is slip velocity, t is slip duration, and a is the fault half width. The displacement is reflected in the velocity and time terms in the second half of the equation, while the shear stress is the product of the friction during sliding and the effective normal stress. High temperatures can only be reached during coseismic slip, when heat generation outpaces heat diffusion along a relatively thin slipping layer (a) within a thicker fault zone. Therefore, evidence of localized high temperatures can be used to identify coseismic slip in exhumed or drilled faults.

Biomarker thermal maturity has proven an effective tool for identifying zones of coseismic slip within a fault zone (Coffey et al., 2019; Polissar et al., 2011; Rabinowitz et al., 2020; Savage & Polissar, 2019; Savage et al., 2014). Biomarkers are the molecular remains of organisms preserved in sedimentary rocks, which when heated, undergo structural changes, rearrangements, or transformations depending upon the thermal stability of the molecules. These molecular changes lead to shifts in abundance of a particular biomarker, or in the ratios of different biomarkers, that can be used to constrain earthquake-heating conditions (Rabinowitz et al., 2017; Savage et al., 2018; Sheppard et al., 2015). The kinetics of biomarker reaction have been established at experimental timescales, from which we can reliably extrapolate to earthquake timescales (Rabinowitz et al., 2017). There is a tradeoff between duration and temperature of heating where higher

10.1029/2021GC009638

temperatures are required for biomarker reaction during shorter events like earthquakes than for burial heating. We define a thermal maturity signal as an increase in the extent of biomarker reaction above the background maturity by at least the two-sigma analytical error. Therefore, placing careful constraints on the background thermal maturity of sediment, which is a function of sediment source and depth of burial, is necessary for accurate interpretation of thermal maturity measurements (Polissar et al., 2011). In this study, we utilize long-chain *n*-alkanes and long-chain unsaturated ketones (alkenones) as they are prevalent at the depths drilled during EXP 372/375.

Long-chain *n*-alkanes are found in the leaf waxes of plants and have a biological preference for odd-numbered carbon chains (Eglinton & Hamilton, 1967; Eglinton et al., 1962). As they are heated, cracking reactions occur and carbon chain lengths become more randomly distributed (Simoneit, 1994), ultimately resulting in a distribution with no preference for odd *n*-alkanes. We can track these changes using the Carbon Preference Index (CPI, Equation 2), which will decrease with increasing temperature rise:

$$\mathrm{CPI} = \frac{C_{25} + C_{27} + C_{29} + C_{31} + C_{33}}{C_{24} + C_{26} + C_{28} + C_{30} + C_{32}} \tag{2}$$

Alkenones are long-chain unsaturated methyl- and ethyl-ketones (MK and EK) produced by the Prymnesiophyceae class of algae. They are used in paleoclimate studies to constrain past sea-surface temperatures because alkenone unsaturation, the number of double bonds in the molecule, decreases with increasing temperature (Brassell et al., 1986; Simoneit, 1994). Alkenones also demonstrate this relationship when heated at earthquake temperatures and durations (Rabinowitz et al., 2017). We focus on changes in the distribution of C_{37} methyl ketones, using $U_{37}^{k'}$:

$$U_{37}^{k'} = \frac{\mathrm{MK}_{37:2}}{\mathrm{MK}_{37:2} + \mathrm{MK}_{37:3}} \tag{3}$$

$U_{37}^{k'}$ increases with temperature due to the faster destruction of the tri-saturated alkenones ($\mathrm{MK}_{37:3}$) relative to di-saturated alkenones ($\mathrm{MK}_{37:2}$). We also look at the concentration of $\mathrm{MK}_{37:3}$ and $\mathrm{MK}_{37:2}$, which we refer to collectively as alkenone concentration. The rate of alkenone destruction increases with increasing temperature and as a result alkenone concentration decreases with higher temperatures and longer duration of heating.

We measured biomarkers in samples at site U1518 to explore the thermal maturity of fault zone rocks. Any samples that contained deformation localization features, both outside and within the fault zone, were subsampled to isolate material from these structures and maximize our ability to detect a heating signal. Based upon the background maturity here and the reaction kinetics of $U_{37}^{k'}$ and CPI we expect biomarker reaction to occur at temperatures of >400°C over earthquake durations. Samples from site U1520, which represent input sediments to the trench, were also measured to establish the background thermal maturity of material from U1518.

Samples were crushed and extracted using a Dionex Accelerated Solvent Extractor (ASE-350) with 9:1 DCM:methanol. 5α-androstane, 1-1′ binapthyl, and stearyl stearate, was added to each total lipid extract (TLE) as a recovery standard. Silica gel column chromatography was used to separate the TLE out into distinct fractions. The aliphatic fraction was eluted using hexane, the ketone/aromatic fraction eluted using dichloromethane, and the polar fraction eluted using methanol. One microliter of each aliphatic fraction was injected and analyzed on an Agilent 7890A gas chromatograph with a 5975C mass selective detector (GC-MSD). The ketone/aromatic fraction was run on a GC-FID using the PTV injector with a 60 m DB1 column. Duplicates of several samples, a blank, and a Hikurangi standard were run at regular intervals during this process to ensure consistency in sample measurements. Alkenone chromatograms were integrated using ChromeQuest software while *n*-alkane chromatograms integrated using ChemStation. Any samples with poor chromatogram quality were either re-run or excluded. More detailed descriptions of methodology and lab procedures can be found in the supporting information.

10.1029/2021GC009638

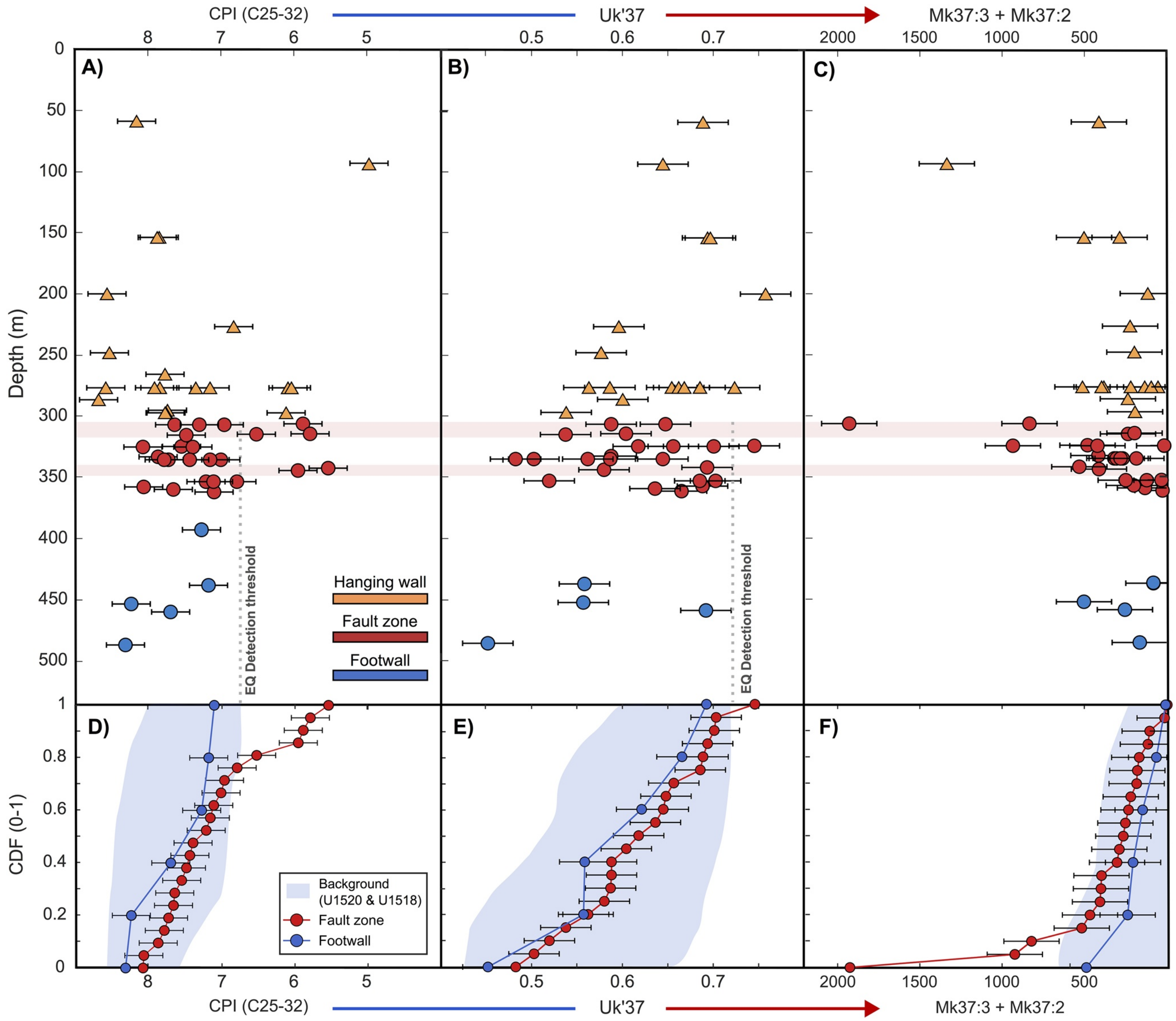

Figure 2. (a–c) Maturity profiles for $U_{37}^{k'}$, Carbon Preference Index (CPI), and alkenone concentration. Points are color coded based upon location in the fault. Error bars are the two-sigma analytical uncertainty. The gray dotted line is earthquake detection threshold. It is absent in (c) because it is below zero due to the background variability and analytical error of alkenones at the Pāpaku fault. Any samples that plot to the right of this line are possible heating signals. We are not plotting an earthquake detection threshold in the hanging wall as we have not constrained the background maturity. (d–f) Cumulative distribution functions for CPI, $U_{37}^{k'}$, and alkenone concentration comparing thermal maturities in U1518. The 99.5% confidence interval, including the analytical uncertainties, of the fault zone background maturities (defined using footwall and U1520 background maturities) are shown in blue shading.

3. Thermal Maturity in the Pāpaku Fault

We identify anomalous heating of individual samples by comparing their molecular biomarker distributions to those of unaltered background samples. At site U1518, we group the hanging wall, fault zone, and footwall sediments separately because these likely have experienced different burial histories and may contain material derived from different sources, which will affect thermal maturity measurements (Figure 2). We use values from the undeformed input sediments at site U1520 for background biomarker distributions, grouping samples that correlate to the biostratigraphic ages of the hanging and fault zone/footwall sediments in U1518 (Crundwell & Woodhouse, 2021). We compare the fault zone in U1518 (i.e., at depths >304 mbsf) to equivalent age samples between 220 and 270 mbsf in U1520, as these likely reflect similar depositional settings. In addition, we also use the thermal maturity of the footwall in U1518 to define the

10.1029/2021GC009638

background of the fault zone, as the fault zone consists of footwall-derived sediments and is undeformed (Figure S1).

The hanging wall of U1518 contains sediments deposited from 650 to 530 ka. This corresponds to only a narrow depth interval in U1520 (391–416 mbsf), where we have a single measurement of background thermal maturity. With only a single background sample as well as large variations in biomarker maturity in the hanging wall more generally, we are unable to differentiate thermally altered samples from normal variability. Therefore, we focus on detecting thermal maturation and heating signatures in the fault zone of U1518.

Variations in background sample maturity reflect variations in the original sediments and any subsequent heating from burial. At the low temperatures encountered here (~10°C at 300 mbsf in U1518; Wallace et al., 2019), thermal maturation from burial is not a factor. However, variations in the background values do occur because of natural variability in the source of the molecules at the time of deposition (e.g., sea surface temperature change, source of turbidites, etc.). Turbidites are abundant in U1518 (Wallace et al., 2019) and can transport inputs from numerous sources to the core site (Chough, 1984; Frenz et al., 2009; Jaeger et al., 2019; Perri et al., 2012). Therefore, the high variability in the background thermal maturity is likely a consequence of variability in the source of the sediment supply to the Hikurangi margin over time (Peters et al., 2005).

We identify samples as anomalously heated if their thermal maturity exceeds the most mature background sample plus our two-sigma analytical uncertainty (i.e., they plot to the right of the earthquake detection threshold in Figure 2). Samples that plot below this threshold (i.e., to the left of the earthquake detection threshold in Figure 2) are interpreted to fall within background maturity. This approach is conservative and likely misses some samples that were heated but did not react sufficiently to exceed the highest values of the background samples. However, we can be confident that we are identifying samples that fall outside of the distribution of background samples and have experienced coseismic heating. Typically, we evaluate heating in a sample by the progressive maturation above background in $MK_{37:2+37:3}$, followed by $U_{37}^{k'}$ and CPI at higher temperatures (Rabinowitz et al., 2020). However, at Hikurangi, the ranges of alkenone concentration parameters $MK_{37:2+37:3}$ and $U_{37}^{k'}$ background values are large and therefore the CPI reaction extent is the first to exceed the background values. In the case of alkenone concentration (Figure 2c), variation in background and the analytical error of these measurements mean that the earthquake detection threshold is below or near to zero. Therefore, we cannot confidently distinguish earthquake-heating signals from background using alkenone concentration and focus instead on CPI and $U_{37}^{k'}$.

Finally, we compare the distribution of fault zone versus background biomarker thermal maturity values using cumulative distribution functions (CDFs). Differences in CDFs can reveal systematic increases from heating that did not exceed the maximum background values. For example, the "cool" tail of fault-zone samples could be systematically more thermally mature than background samples even if the most mature samples in the fault-zone and background samples are similar (Savage & Polissar, 2019). We estimate the sampling uncertainty on our background distributions using bootstrap resampling (Figures 2d–2f) and look for parts of the fault-zone distribution that exceeds this uncertainty.

Four CPI measurements from within the Pāpaku fault zone (305.70, 313.85, 341.82, and 343.75 mbsf) plot above the detection threshold and are identified as coseismic heating signals. The CDFs of *n*-alkane CPI show these samples as anomalous compared to background samples, as well as the rest of the fault zone samples (Figure 2d). The four heated samples were collected from regions where brittle and ductile structures, such as faults and flow bands, are prominent. The shallowest sample (PP2799; Figure 3a) is located ~1 m from the boundary between the top of the fault zone and the hanging wall, within a highly deformed, breccia unit. The next deepest sample (PP2801; Figure 3b) was located within an intensely deformed interval of the core, interpreted as faulted, consisting of incoherent sediment and located at a transition between highly brecciated material above and truncated silt beds below (Fagereng et al., 2019). The two deepest samples within the fault (PP2803 and PP2773; Figures 3c and 3d), are not associated with significant brittle deformation, however they are located in areas of abundant ductile deformation, from processes such as macroscopic flow of sediments and localized extension, with flow banding and dismembered bedding present throughout this interval (Fagereng et al., 2019). We are unable to identify any anomaly in $U_{37}^{k'}$ for these four sample above background (due to the large range of background values). However, these values of $U_{37}^{k'}$

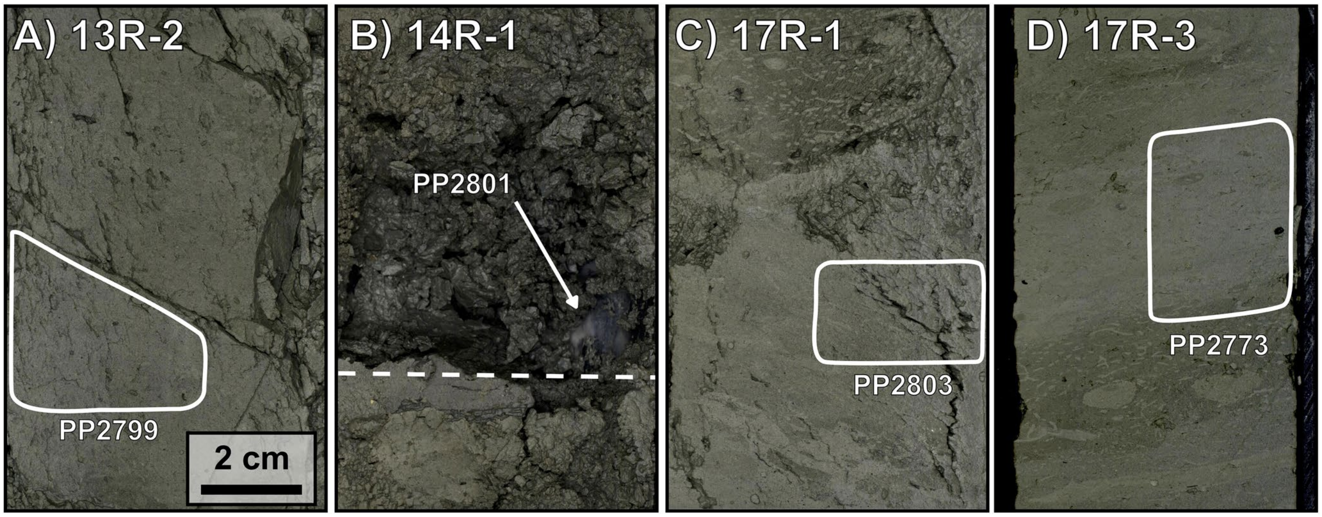

Figure 3. Core photos of the four samples in the fault zone (a–d) demonstrating evidence of reaction. (a) Sample collected in a region of abundant fracturing, (b) sample collected at a boundary (dashed line) between more ductile deformation (above) and brittle deformation, including truncated beds (below), (c and d) samples collected in regions of the core that are dominated by ductile deformation. Bioturbation and flow bands can be seen.

are consistent with the substantial coseismic heating that produces the observed CPI anomalies, if they started from less mature values of $U_{37}^{k'}$.

4. Thermal Modeling of Coseismic Temperature Rise

Temperature-dependent reaction kinetics allow us to constrain the coseismic heating needed to produce the biomarker thermal maturity in the fault zone. When modeling coseismic temperature rises, we assume that all reaction occurred during a single earthquake. This is based upon previous work which has shown that a thermal maturity signal is dominated by the largest earthquake the fault has experienced (Coffey et al., 2019). Although smaller earthquakes can, and probably do, enhance the thermal maturity to some extent, our approach allows us to determine the largest possible earthquake that could have generated the thermal anomaly in our data set. Our model procedure is summarized in Figure 4. First, we use heat generation and diffusion equations (Carslaw & Jaeger, 1959; Lachenbruch, 1986) to forward model coseismic temperature rise across a fault for a range of possible fault geometry and slip conditions (Figure 4a). Coseismic temperature rise within the fault zone is described as:

$$\Delta T\left(x < a, t\right) = \frac{\tau}{\rho c_p}\frac{v}{2a}\left\{\begin{array}{c} t\left[1 - 2i^2 erfc\dfrac{a-x}{\sqrt{4\alpha t}} - 2i^2 erfc\dfrac{a+x}{\sqrt{4\alpha t}}\right] - \\ H\left(t-t^*\right)\left(t-t^*\right)\left[1 - 2i^2 erfc\dfrac{a-x}{\sqrt{4\alpha\left(t-t^*\right)}} - 2i^2 erfc\dfrac{a+x}{\sqrt{4\alpha\left(t-t^*\right)}}\right]\end{array}\right\} \quad (4)$$

where x is distance from the midpoint of the fault, t is time, $t*$ is the duration of the event, τ is shear stress, v is slip velocity, a is the half-width of the slip layer, ρ is density, c_p is heat capacity, δ is thermal diffusivity, and i^2erfc is the second integral of the complementary error function. $H\left(\varsigma\right)$ is the Heaviside function evaluated for $\varsigma = t - t^*$. Parameters used in this calculation can be found in Table 1. Outside of the actively slipping layer, temperature rise is described as:

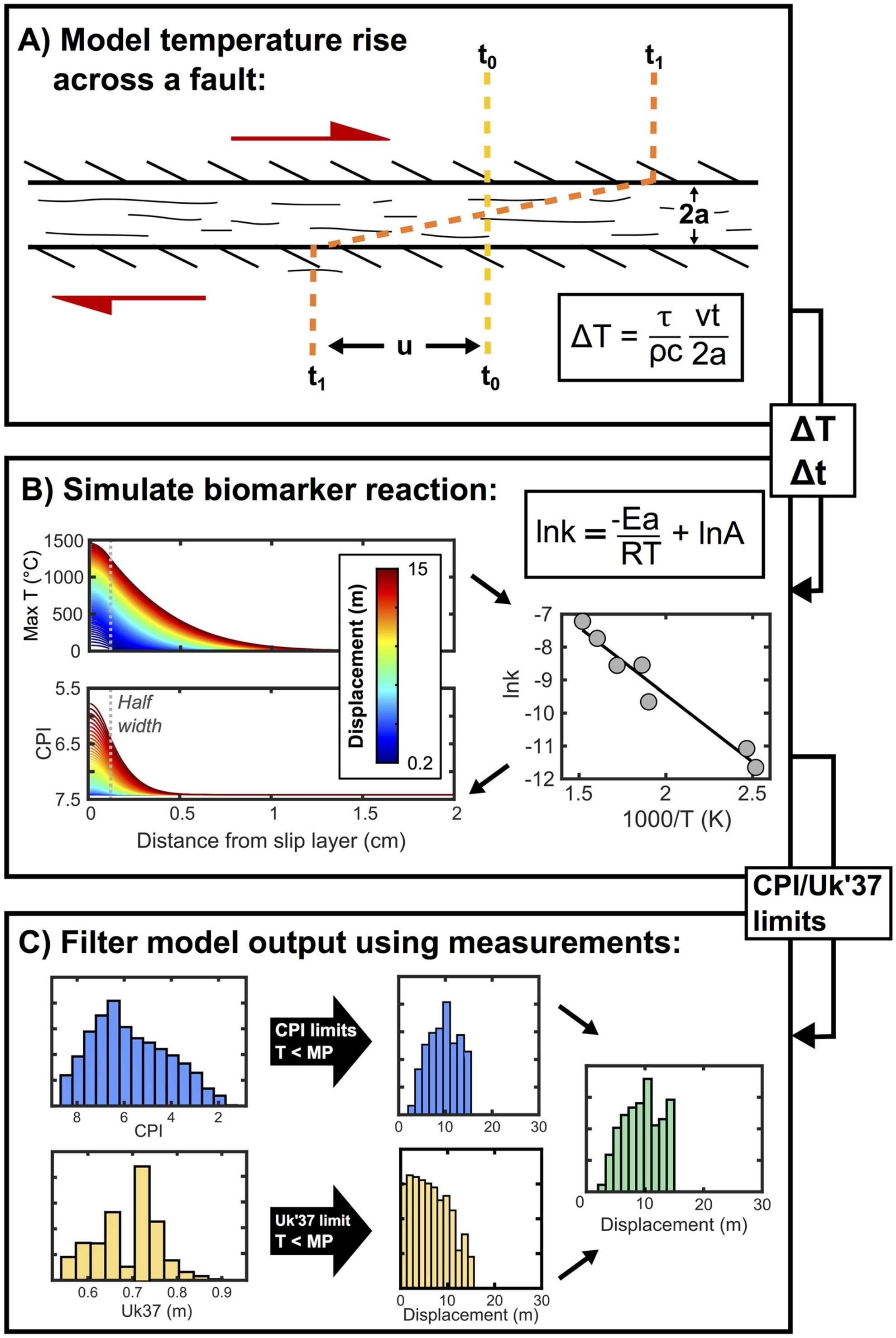

Figure 4. Modeling procedure to determine temperature rise (ΔT) and displacement (vt) for reacted samples. (a) Modeling heat generation and diffusion across a fault from the beginning (t0) to end (t1) of sliding. (b) Forward modeling maximum temperature and biomarker reaction (Carbon Preference Index [CPI]) by coupling time and temperature conditions from (a) with the reaction kinetics (Ea and A) for each biomarker. (c) Identifying the biomarker reaction profiles that are consistent with the measured values for the reacted samples and that result from temperatures below the melting point (MP) of clay.

Table 1
Parameters Used to Model the Temperature Rise Experienced by Coseismically Heated Samples in U1518

Fault property	Model parameter	Source
Peak friction	0.65	Aretusini et al. (2021); this study (Table S2)
High velocity steady-state friction	0.3	Aretusini et al. (2021)
Density (kg m^{-3})	1,800	Wallace et al. (2019)
Heat capacity (J Kg^{-1} K^{-1})	760	Lin et al. (2014)
Thermal diffusivity (m^2 s^{-1})	1×10^{-6}	Wallace et al. (2019)
Effective normal stress (MPa)	2.4	This study
Displacement (m)	0.2–30	This study
Slip-layer thickness (mm)	0.100–2	This study
Velocity (m s^{-1})	0.2–1	Heaton (1990), Bell et al. (2014)

$$\Delta T\left(x > a, t\right) = \frac{\tau}{\rho c_p}\frac{v}{2a}\left\{\begin{array}{c} t\left[2i^2 erfc\frac{x-a}{\sqrt{4\alpha t}} - 2i^2 erfc\frac{x+a}{\sqrt{4\alpha t}}\right] - \\ H\left(t-t^*\right)\left(t-t^*\right)\left[2i^2 erfc\frac{x-a}{\sqrt{4\alpha\left(t-t^*\right)}} - 2i^2 erfc\frac{x+a}{\sqrt{4\alpha\left(t-t^*\right)}}\right]\end{array}\right\} \tag{5}$$

From these equations, we can calculate time-temperature histories for different earthquake scenarios (Figure 4b). To do this, we assume that during the event, conditions change in one dimension across the fault, heat is transferred only by conduction, slip velocity and fault width are constant, and deformation in the fault zone is homogenous. Because friction evolves with sliding over some thermal weakening distance, we calculate the average friction as a function of displacement. To do this, we calculate friction at each point ($n = 1{,}000$) during an event's total displacement using peak and steady-state friction values derived from experiments on samples from the turbidite sequences surrounding the Pāpaku fault (Aretusini et al., 2021; Di Toro et al., 2011; Seyler et al., 2020). Larger displacements are associated with lower average friction as these events spend more time sliding at a lower, dynamically weakened friction (see Methods in the supporting information). We explore slip velocities between 0.2 and 1 m/s to cover a spectrum of slip velocities from slower-rupturing tsunami earthquakes to regular coseismic slip. These and other modeling parameters are outlined in Table 1. Slip-layer thickness, displacement, slip velocity, and friction are modeled as uniform distributions to propagate uncertainties using a Monte Carlo approach.

We then simulate the change in $U_{37}^{k'}$, CPI, and alkenone concentration for each of these time-temperature histories. The reaction in each of these thermal maturity parameters can be described using a first-order Arrhenius equation:

$$\ln k = Ae^{\frac{E_a}{RT}} \tag{6}$$

where R is the ideal gas constant, T is temperature in Kelvin, and k is the rate constant. A and E_a are the experimentally determined frequency factor and activation energy for the reaction of each biomarker (Rabinowitz et al., 2017). A Monte Carlo approach is used to propagate uncertainties in A and E_a. Parametric bootstrapping is used to generate a population of A-E_a pairs that fit the reaction kinetics for each biomarker and each A-E_a pair is coupled with each time-temperature history to compute biomarker reaction profiles that reflect all uncertainties in the data (Figure 4b). Finally, we filter the modeled biomarker results to eliminate all profiles that do not agree with the measured thermal maturity data (Figures 4c and S3). Cases where temperature rise is greater than 1100°C are also removed, as this is above the melting temperature of most clays (Srinivasachar et al., 1990) and no evidence of melting has been observed in the core to date. The final result is a distribution of possible fault parameters that can produce the observed biomarker signals and therefore constrain earthquake properties.

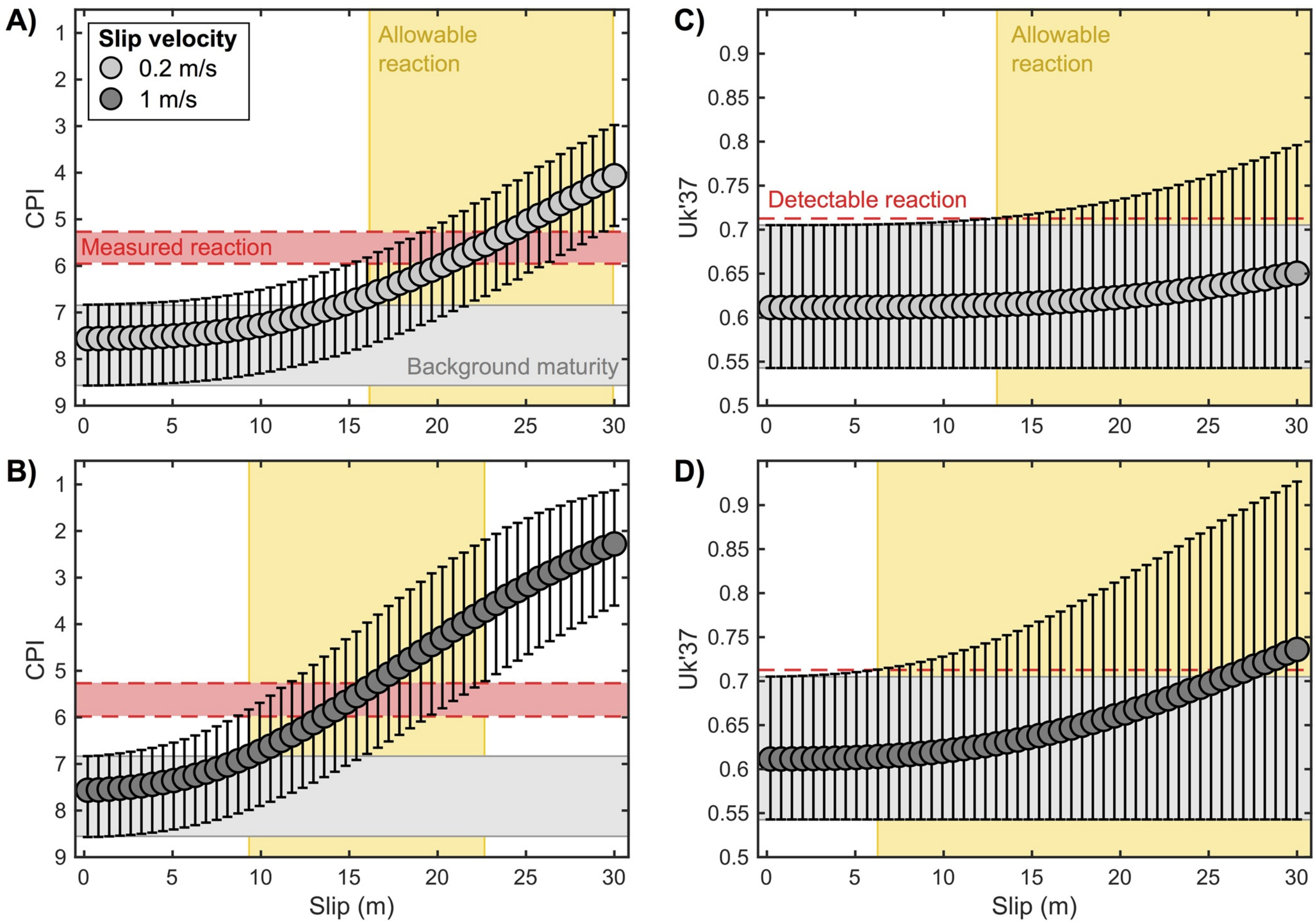

Figure 5. Biomarker reaction with displacement for slip velocities of 0.2 and 1 m/s and reaction in the fault zone. Gray shaded regions show the range of background maturities for each biomarker. Red shaded areas show the measured range of thermal maturities in thermally altered samples from the fault. For $U_{37}^{k'}$ where reaction was not observed, the red dashed line indicates the minimum amount of reaction required to produce a thermal-maturity signal above background. Yellow shaded regions represent maturities and hence displacements that are consistent with our measurements and are used to constrain minimum bounds on displacement. The variability in alkenone concentration means that we cannot constrain displacement as any reaction that occurs will lead to alkenone concentrations that fall within the background range. The overlap of yellow areas in (a and c) or (b and d) indicate the range of slip values allowed by the biomarker results for slip velocities of 0.2 and 1 m/s, respectively. Plots for alkenone concentration can be found in the supporting information.

5. Pāpaku Fault Earthquakes

5.1. Constraints on Possible Earthquake Displacements

We identify evidence of coseismic heating in the CPI of four samples from within the Pāpaku fault zone (Figure 2). Alkenones and *n*-alkanes have different reaction kinetics and therefore, will not react to the same extent during the same heating conditions. This is illustrated for the fault zone samples in Figure 5, where we have modeled the reaction that occurs for each CPI, $U_{37}^{k'}$, and alkenone concentration for a range of earthquake parameters outlined in Table 1. We modeled slip velocities of 0.2 and 1 m/s to simulate reaction during slower-rupturing events, such as tsunami earthquakes, and regular-speed coseismic slip events (Bell et al., 2014; Heaton, 1990). Slower slip velocities, for example, during SSEs, do not generate high enough temperatures to cause biomarker reaction as heat generation is outpaced by diffusion into surrounding wall rock in narrow slip layers. It is also worth noting that we do not expect drilling-induced deformation or hydrothermal fluid flow to generate the observed heating signals. Drilling-induced deformation should only affect material closest to biscuit boundaries, which were avoided during sampling, while hydrothermal fluids at this location are <100°C (Barnes et al., 2010; Cook et al., 2020), which is below what would be required for biomarker reaction here. Furthermore, we do not see a correlation between heating anomalies and fracture density (Savage et al., 2021), which we may expect if fluids or methane

10.1029/2021GC009638

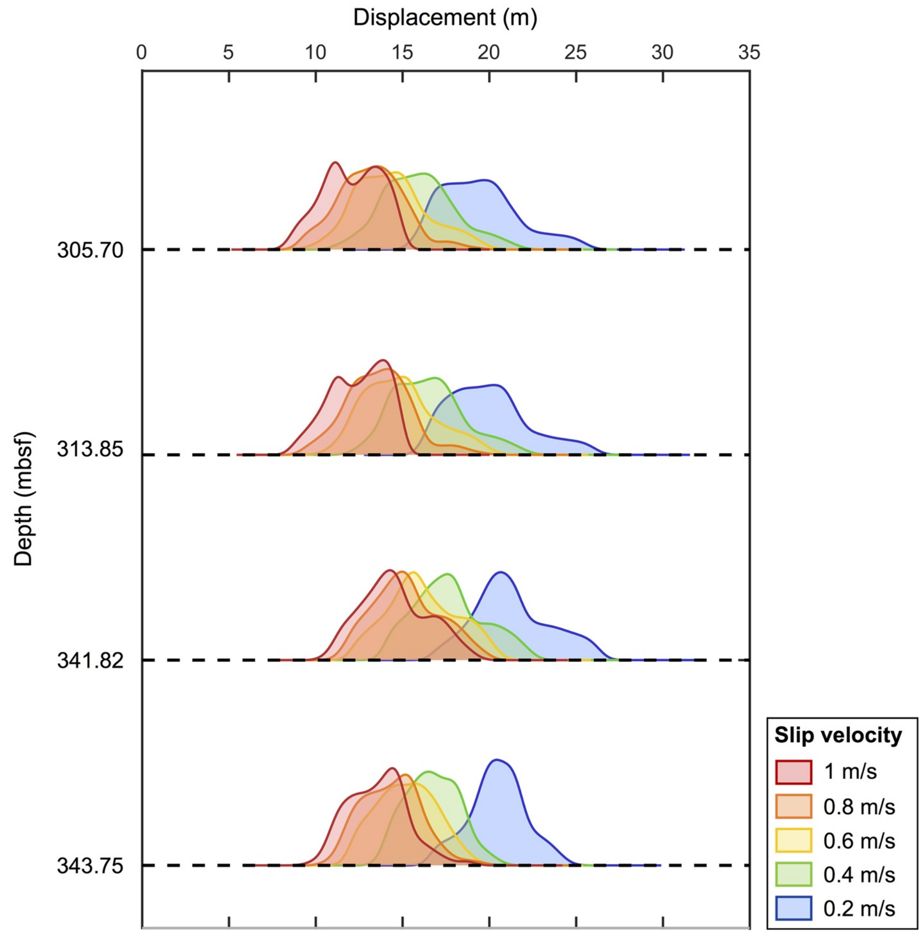

Figure 6. Probability density functions (PDFs) for each sample that shows evidence of reaction plotted according to slip velocity. The *y*-axis scale is the same for all PDFs.

were influencing thermal maturity. From our results, it is clear that CPI reaction can be distinguished from background maturity at lower temperatures and displacements than for $MK_{37:2+37:3}$ or $U_{37}^{k'}$ (Figures 5a–5d). Therefore, we can use the differences in kinetics of $MK_{37:2+37:3}$, $U_{37}^{k'}$, and CPI to place constraints on possible earthquake displacements along and near the Pāpaku fault.

5.2. Earthquake Displacement Distributions

In addition to illustrating the relationship between displacement and reaction for each of the biomarker parameters in Figure 5, we create probability density functions of displacement using all the possible earthquakes modeled for each reacted sample in U1518. We can then identify the most probable displacements during each event (Figure 6, Table 2). For a 1 m/s earthquake, the highest probability displacements for each sample range between 14.0 and 14.9 m, while for lower slip velocities (i.e., <1 m/s), these fall between 15.0 and 21.0 m. Overall, at slip velocities of between 0.8 and 1 m/s, the most likely displacements are higher than displacements from paleoseismic studies of terraces and subsidence along the Hikurangi margin (Berryman et al., 1989; Clark et al., 2019; Ota et al., 1990; Wilson et al., 2007). However, our estimates are for slip on a dipping plane, while paleoseismology constraints are on vertical displacements and hence, smaller. As a result, our estimates of displacement are comparable to paleoseismic displacements. Slower earthquakes are less likely due to the large displacements required to fit the data. While we have been assuming that this signal results from the largest earthquake, the fault has experienced according to Coffey et al. (2019), contributions from multiple moderate earthquakes (e.g., $>M_w$ 6) could also lead to the observed thermal signal, in which case the largest earthquake would be somewhat smaller.

10.1029/2021GC009638

Table 2
Most Likely Displacements for Each Sample That Shows Evidenced of Reaction and Each Slip Velocity Modeled

		Most probable displacement (m) according to slip velocity (m/s)				
Sample ID	Depth	0.2	0.4	0.6	0.8	1
PP2799	305.70	20.4	17.2	15.4	17.2	14.0
PP2801	313.85	20.8	17.7	15.8	15.2	14.3
PP2803	341.82	21.0	17.8	16.3	15.6	14.9
PP2773	343.75	20.7	17.6	15.6	15.0	14.3

5.3. Implications for Seismic Slip Along Splay Faults

Heating signals detected using biomarker thermal maturity measurements were found at four different locations within the Pāpaku fault zone. These data suggest that multiple earthquakes have propagated along the Pāpaku fault and/or that earthquake rupture was branching and occurred along multiple strands as has been demonstrated in other places (Meng et al., 2012; Park et al., 2002; Rabinowitz et al., 2020). It is also likely that earthquakes occurred elsewhere within the fault and were either not sampled or their signal was obscured by the variation in background maturity. We see that the evidence for earthquake slip is not necessarily restricted to the obvious brittle deformation features in a fault but have also can be detected in regions of ductilely deformed sediment. However, some of ductile structures here are formed by granular flow and may be associated with frictional heating during slip (Adam et al., 2005; Fagereng et al., 2019). Alternatively, later overprinting and reworking of formerly brittlely deformed sediments may have occurred during slower slip obscuring earlier brittle structures.

Our results confirm that the Pāpaku fault has hosted earthquake slip within its shallow reaches. While slower slip may also occur here (Fagereng et al., 2019), our results demonstrate that the fault has relieved at least some component of its accumulated strain during earthquake events. While we cannot rule out that slower earthquakes are responsible for the thermal maturity signal observed here, we think that slip velocities of 0.4 m/s or less are very unlikely as while heat is still being produced during slip, displacements required to fit the data are likely too large. Given that the Pāpaku fault intersects the seafloor, is more steeply dipping than the megathrust (Fagereng et al., 2019), and hosts coseismic displacements of at least 14 m at shallow depths (Figure 5), the Pāpaku fault was likely tsunamigenic in the past and it and other splay faults along the Hikurangi margin should be associated with high tsunami hazard.

In addition to constraining maximum earthquake size, we can quantify the range of frictional energy dissipated during slip. Quantifying frictional energy allows us to constrain aspects of the earthquake energy budget and therefore, better understand the energy available for rupture propagation (Kanamori & Rivera, 2006). Fracture and radiated energy, the two other major components of the earthquake energy budget, can be measured from seismograms. The energy dissipated due to frictional heating however, requires alternative means to be quantified and only a handful of estimates exist. We calculate frictional energy using the range of possible displacements constrained from biomarkers according to the following equation:

$$F_w = \tau d$$

The mean frictional energy at the Pāpaku fault is 10.6 MJ/m^2 (95% confidence interval of 8–13 MJ/m^2), which falls at the low end of the handful of estimates that currently exist (~2–228 MJ/m^2; e.g., Coffey et al., 2019; Fulton et al., 2019; Pittarello et al., 2008; Savage & Polissar, 2019; Savage et al., 2014). Frictional energy was estimated from fault temperature measured after the Tohoku-oki earthquake at 20–86 MJ/m^2 (Brodsky et al., 2019; Fulton et al., 2013). The lower estimates of frictional energy required at Hikurangi reflects both the slightly greater depth of the measurement at JFAST as well as the much larger displacement (50–70 m) that occurred near the seafloor during the Tohoku-oki earthquake.

6. Conclusions

Biomarker thermal maturity measurements in the Pāpaku fault show a clear thermal maturity signal in four samples, indicating that earthquakes propagate to shallow depth within the Hikurangi deformation front. These slip events are large, and the most likely displacements fall between 14 and 17 m for slip velocities of 0.8–1 m/s. Lower slip velocities require larger, less likely, displacements. Biomarkers provide evidence that splay faults are accommodating strain along the Hikurangi margin through earthquakes ($M_w > 7$), and not purely through slow slip or aseismic creep. Our results are the first direct evidence of large coseismic displacements along an offshore splay fault of the Hikurangi subduction zone. Along with the large, very shallow displacements modeled for these events and steep dip (≤30°) of the Pāpaku fault relative to the underlying megathrust (Wallace et al., 2019), our results indicate that the Pāpaku fault is capable of producing large tsunamis during an earthquake. Therefore, splay faults deserve particular attention when considering the tsunamigenic potential of a region and the risk they pose to coastal communities like those on the east coast of New Zealand.

Data Availability Statement

Data supporting these conclusions can be found within tables in the manuscript and in the EarthChem repository (https://doi.org/10.26022/IEDA/112023).

Acknowledgments

G. L. Coffey and the biomarker measurements were supported by an award from the U.S. Science Support Program/International Discovery Program (NSF-OCE 1450528) to H. M. Savage. G. L. Coffey was also supported by the Brinson Foundation. The authors would like to thank the science, technical, and operational crew of IODP EXP375 for their contributions toward the collection of these data. The authors are also grateful for help the help of Nicole deRoberts and Wei Huang for assistance with lab analyses.

References

Adam, J., Urai, J. L., Wieneke, B., Oncken, O., Pfeiffer, K., Kukowski, N., et al. (2005). Shear localisation and strain distribution during tectonic faulting—New insights from granular-flow experiments and high-resolution optical image correlation techniques. *Journal of Structural Geology*, *27*(2), 283–301. https://doi.org/10.1016/j.jsg.2004.08.008

Aretusini, S., Meneghini, F., Spagnuolo, E., Harbord, C. W., & Di Toro, G. (2021). Fluid pressurisation and earthquake propagation in the Hikurangi subduction zone. *Nature Communications*, *12*, 2481. https://doi.org/10.1038/s41467-021-22805-w

Barker, D. H. N., Henrys, S., Caratori Tontini, F., Barnes, P. M., Bassett, D., Todd, E., & Wallace, L. (2018). Geophysical constraints on the relationship between seamount subduction, slow slip, and tremor at the North Hikurangi subduction zone, New Zealand. *Geophysical Research Letters*, *45*(23), 12804–12813. https://doi.org/10.1029/2018GL080259

Barnes, P. M., Lamarche, G., Bialas, J., Henrys, S., Pecher, I., Netzeband, G. L., et al. (2010). Tectonic and geological framework for gas hydrates and cold seeps on the Hikurangi subduction margin, New Zealand. *Marine Geology*, *272*(1–4), 26–48. https://doi.org/10.1016/j.margeo.2009.03.012

Barnes, P. M., Wallace, L. M., Saffer, D. M., Bell, R. E., Underwood, M. B., Fagereng, A., et al. (2020). Slow slip source characterized by lithological and geometric heterogeneity. *Science Advances*, *6*(13), 1–11. https://doi.org/10.1126/sciadv.aay3314

Bécel, A., Shillington, D. J., Delescluse, M., Nedimović, M. R., Abers, G. A., Saffer, D. M., et al. (2017). Tsunamigenic structures in a creeping section of the Alaska subduction zone. *Nature Geoscience*, *10*(8), 609–613. https://doi.org/10.1038/NGEO2990

Bell, R., Holden, C., Power, W., Wang, X., & Downes, G. (2014). Hikurangi margin tsunami earthquake generated by slow seismic rupture over a subducted seamount. *Earth and Planetary Science Letters*, *397*, 1–9. https://doi.org/10.1016/j.epsl.2014.04.005

Bell, R., Sutherland, R., Barker, D. H. N., Henrys, S., Bannister, S., Wallace, L., & Beavan, J. (2010). Seismic reflection character of the Hikurangi subduction interface, New Zealand, in the region of repeated Gisborne slow slip events. *Geophysical Journal International*, *180*(1), 34–48. https://doi.org/10.1111/j.1365-246X.2009.04401.x

Berryman, K. R., Ota, Y., & Hull, A. G. (1989). Holocene paleoseismicity in the fold and thrust belt of the Hikurangi subduction zone, eastern North Island, New Zealand. *Tectonophysics*, *163*, 185–195. https://doi.org/10.1016/0040-1951(89)90256-4

Berryman, K. R., Ota, Y., Miyauchi, T., Hull, A., Clark, K., Ishibashi, K., et al. (2011). Holocene paleoseismic history of upper-plate faults in the southern Hikurangi subduction margin, New Zealand. *Deduced from Marine Terrace Records*, *101*(5), 2064–2087. https://doi.org/10.1785/0120100282

Bilek, S. L., & Lay, T. (2002). Tsunami earthquakes possibly widespread manifestations of frictional conditional stability. *Geophysical Research Letters*, *29*(14), 18-1–18-4. https://doi.org/10.1029/2002gl015215

Brassell, S. C., Eglinton, G., Marlowe, I. T., Pflaumann, U., & Sarnthein, M. (1986). Molecular stratigraphy: A new tool for climatic assessment. *Nature*, *320*(6058), 129–133. https://doi.org/10.1038/320129a0

Brodsky, E. E., Mori, J. J., Anderson, L., Chester, F. M., Conin, M., Dunham, E. M., et al. (2020). The state of stress on the fault before, during, and after a major earthquake. *Annual Review of Earth and Planetary Sciences*, *48*, 49–74. https://doi.org/10.1146/annurev-earth-053018-060507

Carslaw, H. S., & Jaeger, J. C. (1959). *Conduction of heat in solids* (2nd ed.). Clarendon Press.

Chough, S. K. (1984). Fine-grained turbidites and associated mass-flow deposits in the Ulleung (Tsushima) Back-arc Basin, East Sea (Sea of Japan) S.K. Chough. *Geological Society, London, Special Publications*, *15*, 185–196. https://doi.org/10.1144/gsl.sp.1984.015.01.12

Clark, K., Howarth, J., Litchfield, N., Cochran, U., Turnbull, J., Dowling, L., et al. (2019). Geological evidence for past large earthquakes and tsunamis along the Hikurangi subduction margin, New Zealand. *Marine Geology*, *412*, 139–172. https://doi.org/10.1016/j.margeo.2019.03.004

Coffey, G. L., Savage, H. M., Polissar, P. J., Rowe, C. D., & Rabinowitz, H. S. (2019). Hot on the trail: Coseismic heating on a localized structure along the Muddy Mountain fault, Nevada. *Journal of Structural Geology*, *120*, 67–79. https://doi.org/10.1016/j.jsg.2018.12.012

Cook, A. E., Paganoni, M., Clennell, M. B., McNamara, D. D., Nole, M., Wang, X., et al. (2020). Physical properties and gas hydrate at a near-seafloor thrust fault, Hikurangi margin, New Zealand. *Geophysical Research Letters*, *47*(16), 1–11. https://doi.org/10.1029/2020GL088474

Crundwell, M., & Woodhouse, A. (2021). *Crundwell & Woodhouse (Quaternary biostrat): Appendices, supplementary appendices, and supplementary material*. Figshare, Journal contribution. https://doi.org/10.6084/m9.figshare.13604630.v1

Di Toro, G., Han, R., Hirose, T., De Paola, N., Nielsen, S., Mizoguchi, K., et al. (2011). Fault lubrication during earthquakes. *Nature*, *471*(7339), 494–498. https://doi.org/10.1038/nature09838

Eglinton, G., Gonzalez, A. G., Hamilton, R. J., & Raphael, R. A. (1962). Hydrocarbon constituents of the wax coatings of plant leaves: A taxonomic survey. *Phytochemistry*, *1*(2), 89–102. https://doi.org/10.1016/S0031-9422(00)88006-1

Eglinton, G., & Hamilton, R. J. (1967). Leaf epicuticular waxes. *Science*, *156*, 1322–1335. https://doi.org/10.1126/science.156.3780.1322

Fagereng, Å., Savage, H. M., Morgan, J. K., Wang, M., Meneghini, F., & Barnes, P. M. (2019). Mixed deformation styles on a shallow subduction thrust, Hikurangi margin, New Zealand. *Geology*, *47*(9), 872–876. https://doi.org/10.1130/G46367.1

Frenz, M., Wynn, R. B., Georgiopoulou, A., Bender, V. B., Hough, G., Masson, D. G., et al. (2009). Provenance and pathways of late Quaternary turbidites in the deep-water Agadir Basin, northwest African margin. *International Journal of Earth Sciences*, *98*, 721–733. https://doi.org/10.1007/s00531-008-0313-4

Fulton, P. M., Brodsky, E., Kano, Y., Mori, J., Chester, F., Ishikawa, T., et al. (2013). Low coseismic friction on the Tohoku-oki fault determined from temperature measurements. *Science*, *6153*, 1214–1217. https://doi.org/10.1126/science.1243641

Fulton, P. M., Brodsky, E., Mori, J. J., & Chester, F. M. (2019). Tōhoku-oki fault zone frictional heat measured: During IODP expeditions 343 and 343t. *Oceanography*, *32*(1), 102–104. https://doi.org/10.5670/oceanog.2019.129

Hayman, N. W., Toshiya, K., Lisa C, M., Kyuichi, K., Toshiya, K., Cassandra M, B., et al. (2012). Structural evolution of an inner accretionary wedge and forearc basin initiation, Nankai margin, Japan. *Earth and Planetary Science Letters*, *353*, 163–172. https://doi.org/10.1016/j.epsl.2012.07.040

Heaton, T. H. (1990). Evidence for and implications of self-healing pulses of slip in earthquake rupture. *Physics of the Earth and Planetary Interiors*, *64*, 1–20. https://doi.org/10.1016/0031-9201(90)90002-f

Jaeger, D., Stalder, R., Masago, H., & Strasser, M. (2019). OH defects in quartz as a provenance tool: Application to fluvial and deep marine sediments from SW Japan. *Sedimentary Geology*, *388*, 66–80. https://doi.org/10.1016/j.sedgeo.2019.05.003

Johnson, J. M., & Satake, K. (1997). Estimation of seismic moment and slip distribution of the April 1, 1946, Aleutian tsunami earthquake. *Journal of Geophysical Research*, *102*(B6), 11765–11774. https://doi.org/10.1029/97jb00274

Kanamori, H., & Rivera, L. (2006). Energy partitioning during an earthquake. *Geophysical Monograph Series*, *170*, 3–13.

Kimura, G., Kitamura, Y., Hashimoto, Y., Yamaguchi, A., Shibata, T., Ujiie, K., & Okamoto, S. (2007). Transition of accretionary wedge structures around the up-dip limit of the seismogenic subduction zone. *Earth and Planetary Science Letters*, *255*(3–4), 471–484. https://doi.org/10.1016/j.epsl.2007.01.005

Lachenbruch, A. H. (1986). *Simple models for the estimation and measurement of frictional heating by an earthquake*.

Lin, W., Fulton, P. M., Harris, R. N., Tadai, O., Matsubayashi, O., Tanikawa, W., & Kinoshita, M. (2014). Thermal conductivities, thermal diffusivities, and volumetric heat capacities of core samples obtained from the Japan Trench Fast Drilling Project (JFAST). *Earth, Planets and Space*, *66*(1), 1–11. https://doi.org/10.1186/1880-5981-66-48

McCaffrey, R., Wallace, L. M., & Beavan, J. (2008). Slow slip and frictional transition at low temperature at the Hikurangi subduction zone. *Nature Geoscience*, *1*(5), 316–320. https://doi.org/10.1038/ngeo178

Meng, L., Ampuero, J. P., Stock, J., Duputel, Z., Luo, Y., & Tsai, V. C. (2012). Earthquake in a maze: Compressional rupture branching during the 2012 Mw 8.6 Sumatra earthquake. *Science*, *337*(6095), 724–726. https://doi.org/10.1126/science.1224030

Moore, A. G. F., Bangs, N. L., Taira, A., Kuramoto, S., Pangborn, E., & Tobin, H. J. (2007). Three-dimensional splay fault geometry and implications for tsunami generation. *Science*, *318*, 1128–1131. https://doi.org/10.1126/science.1147195

Obara, K., & Kato, A. (2016). Connecting slowearthquakes to huge earthquakes. *Science*, *353*(6296), 253–257. https://doi.org/10.1126/science.aaf1512

Ota, Y., Hull, A. G., & Berryman, K. R. (1991). Coseismic uplift of holocene marine terraces in the pakarae river area, Eastern North Island, New Zealand. *Quaternary Research*, *35*, 331–346. https://doi.org/10.1016/0033-5894(91)90049-B

Ota, Y., Miyauchi, T., & Hull, A. G. (1990). Holocene marine terraces at aramoana and pourerere, Eastern North Island, New Zealand. *New Zealand Journal of Geology and Geophysics*, *33*(4), 541–546. https://doi.org/10.1080/00288306.1990.10421372

Park, J. O., Tsuru, T., Kodaira, S., Cummins, P. R., & Kaneda, Y. (2002). Splay fault branching along the Nankai subduction zone. *Science*, *297*(5584), 1157–1160. https://doi.org/10.1126/science.1074111

Peng, Z., & Gomberg, J. (2010). An integrated perspective of the continuum between earthquakes and slow-slip phenomena. *Nature Publishing Group*, *3*(9), 599–607. https://doi.org/10.1038/ngeo940

Perri, F., Critelli, S., Dominici, R., Muto, F., Tripodi, V., & Ceramicola, S. (2012). Provenance and accommodation pathways of late Quaternary sediments in the deep-water northern Ionian Basin, southern Italy. *Sedimentary Geology*, *280*, 244–259. https://doi.org/10.1016/j.sedgeo.2012.01.007

Peters, K. E., Walters, C. C., & Moldowan, J. M. (2005). The biomarker guide (1). Cambridge University Press.

Pittarello, L., Di Toro, G., Bizzarri, A., Pennacchioni, G., Hadizadeh, J., & Cocco, M. (2008). Energy partitioning during seismic slip in pseudotachylyte-bearing faults (Gole Larghe Fault, Adamello, Italy). *Earth and Planetary Science Letters*, *269*(1–2), 131–139. https://doi.org/10.1016/j.epsl.2008.01.052

Polissar, P. J., Savage, H. M., & Brodsky, E. E. (2011). Extractable organic material in fault zones as a tool to investigate frictional stress. *Earth and Planetary Science Letters*, *311*(3–4), 439–447. https://doi.org/10.1016/j.epsl.2011.09.004

Pouderoux, H., Proust, J.-N., & Lamarche, G. (2014). Submarine paleoseismology of the northern Hikurangi subduction margin of New Zealand as deduced from Turbidite record since 16 ka. *Quaternary Science Reviews*, *84*, 116–131. https://doi.org/10.1016/j.quascirev.2013.11.015

Rabinowitz, H. S., Kirkpatrick, J. D., Savage, H. M., Polissar, P. J., & Rowe, C. D. (2020). Earthquake slip surfaces identified by biomarker thermal maturity within the 2011 Tohoku-Oki earthquake fault zone. *Nature Communications*, *11*(533), 1–9. https://doi.org/10.1038/s41467-020-14447-1

Rabinowitz, H. S., Polissar, P., & Savage, H. (2017). Reaction kinetics of alkenone and *n*-alkane thermal alteration at seismic timescales. *Geochemistry, Geophysics, Geosystems*, *116*(1), 1–12. https://doi.org/10.1002/2016GC006553

Saffer, D. M., & Wallace, L. M. (2015). The frictional, hydrologic, metamorphic and thermal habitat of shallow slow earthquakes. *Nature Geoscience*, *8*(8), 594–600. https://doi.org/10.1038/ngeo2490

Sakaguchi, A., Chester, F., Curewitz, D., Fabbri, O., Goldsby, D., Kimura, G., et al. (2011). Seismic slip propagation to the updip end of plate boundary subduction interface faults: Vitrinite reflectance geothermometry on integrated ocean drilling program nantro SEIZE cores. *Geology*, *39*(4), 395–398. https://doi.org/10.1130/G31642.1

Savage, H. M., & Polissar, P. J. (2019). Biomarker thermal maturity reveals localized temperature rise from paleoseismic slip along the Punchbowl Fault, CA, USA. *Geochemistry, Geophysics, Geosystems*, *20*, 3201–3215. https://doi.org/10.1029/2019GC008225

Savage, H. M., Polissar, P. J., Sheppard, R., Rowe, C. D., & Brodsky, E. E. (2014). Biomarkers heat up during earthquakes: New evidence of seismic slip in the rock record. *Geology*, *42*(2), 99–102. https://doi.org/10.1130/G34901.1

Savage, H. M., Rabinowitz, H. S., Spagnuolo, E., Aretusini, S., Polissar, P. J., & Di, G. (2018). Biomarker thermal maturity experiments at earthquake slip rates. *Earth and Planetary Science Letters*, *502*, 253–261. https://doi.org/10.1016/j.epsl.2018.08.038

Savage, H. M., Shreedharan, S., Fagereng, Å., Morgan, J. K., Menghini, F., Wang, M., et al. (2021). Asymmetric brittle deformation at the Pāpaku Fault, Hikurangi Subduction Margin, NZ, IODP Expedition 375. *Geochemistry, Geophysics, Geosystems*, e2021GC009662. https://doi.org/10.1029/2021GC009662

Seyler, C. E., Kirkpatrick, J. D., Savage, H. M., Hirose, T., & Faulkner, D. R. (2020). Rupture to the trench? Frictional properties and fracture energy of incoming sediments at the Cascadia subduction zone. *Earth and Planetary Science Letters*, *546*, 116413. https://doi.org/10.1016/j.epsl.2020.116413

Shaddox, H. R., & Schwartz, S. Y. (2019). Subducted seamount diverts shallow slow slip to the forearc of the northern Hikurangi subduction zone, New Zealand. *Geology*, *47*(5), 415–418. https://doi.org/10.1130/G45810.1

Sheppard, R. E., Polissar, P. J., & Savage, H. M. (2015). Organic thermal maturity as a proxy for frictional fault heating: Experimental constraints on methylphenanthrene kinetics at earthquake timescales. *Geochimica et Cosmochimica Acta*, *151*, 103–116. https://doi.org/10.1016/j.gca.2014.11.020

Sibson, R. H. (1975). Generation of pseudotachylyte by ancient seismic faulting. *Geophysical Journal of the Royal Astronomical Society*, *43*, 775–794. https://doi.org/10.1111/j.1365-246x.1975.tb06195.x

Simoneit, B. R. T. (1994). Lipid/bitumen maturation by hydrothermal activity in sediments of Middle Valley, Leg 139. *Proceedings of the Ocean Drilling Program, Scientific Results*, *139*, 447–465. https://doi.org/10.2973/odp.proc.sr.139.237.1994

Srinivasachar, S., Helble, J. J., Boni, A. A., Shah, N., Huffman, G. P., & Huggins, F. E. (1990). Mineral behavior during coal combustion 2. Illite transformations. *Progress in Energy and Combustion Science*, *16*(4), 293–302. https://doi.org/10.1016/0360-1285(90)90038-5

Wallace, L. M., & Beavan, J. (2010). Diverse slow slip behavior at the Hikurangi subduction margin, New Zealand. *Journal of Geophysical Research*, *115*(12). https://doi.org/10.1029/2010JB007717

Wallace, L. M., Beavan, J., McCaffrey, R., & Darby, D. (2004). Subduction zone coupling and tectonic block rotations in the North Island, New Zealand. *Journal of Geophysical Research*, *109*(12). https://doi.org/10.1029/2004JB003241

Wallace, L. M., Reyners, M., Cochran, U., Bannister, S., Barnes, P. M., Berryman, K., et al. (2009). Characterizing the seismogenic zone of a major plate boundary subduction thrust: Hikurangi Margin, New Zealand. *Geochemistry, Geophysics, Geosystems*, *10*(10). https://doi.org/10.1029/2009GC002610

Wallace, L. M., Saffer, D. M., Barnes, P. M., Pecher, I. A., Petronotis, K. E., LeVay, L. J., & Scientists, E. (2019). Hikurangi subduction margin coring, logging, and observatories (372B/375). Proceedings of the International Ocean Discovery Program. https://doi.org/10.14379/iodp.proc.372b375.2019

Wallace, L. M., Webb, S. C., Ito, Y., Mochizuki, K., Hino, R., Henrys, S., et al. (2016). Slowslip near the trench at the Hikurangi subduction zone, New Zealand. *Science*, *352*(6286), 701–704. https://doi.org/10.1126/science.aaf2349

Wang, K., & Bilek, S. L. (2014). Invited review paper: Fault creep caused by subduction of rough seafloor relief. *Tectonophysics*, *610*, 1–24. https://doi.org/10.1016/j.tecto.2013.11.024

Wech, A. G., & Creager, K. C. (2011). A continuum of stress, strength and slip in the Cascadia subduction zone. *Nature Geoscience*, *4*(9), 624–628. https://doi.org/10.1038/ngeo1215

Wendt, J., Oglesby, D. D., & Geist, E. L. (2009). Tsunamis and splay fault dynamics. *Geophysical Research Letters*, *36*(15), 1–5. https://doi.org/10.1029/2009GL038295

Wilson, K., Berryman, K., Cochran, U., & Little, T. (2007). Early Holocene paleoseismic history at the Pakarae locality, eastern North Island, New Zealand, inferred from transgressive marine sequence architecture. *Tectonics*, *26*(4), 1–18. https://doi.org/10.1029/2006TC002021

Wilson, K., Berryman, K., Litchfield, N., & Little, T. (2006). A revision of mid-late holocene marine terrace distribution and chronology at the pakarae river mouth, North Island, New Zealand. *New Zealand Journal of Geology and Geophysics*, *49*(4), 477–489. https://doi.org/10.1080/00288306.2006.9515182

References From the Supporting Information

Ikari, M. J., & Kopf, A. J. (2017). Seismic potential of weak, near-surface faults revealed at plate tectonic slip rates. *Science Advances*, *3*(11), e1701269.

Seyler, C. E., Kirkpatrick, J. D., Savage, H. M., Hirose, T., & Faulkner, D. R. (2020). Rupture to the trench? Frictional properties and fracture energy of incoming sediments at the Cascadia subduction zone. *Earth and Planetary Science Letters*, *546*, 116413. https://doi.org/10.1016/j.epsl.2020.116413